



Electron-donating-accepting behavior between nitrogen-doped carbon materials and Fe species and its promotion for DBT hydrodesulfurization



Lei Li^a, Minjian Wang^a, Lingxiang Huang^b, Xuandong Liu^a, Xinyue Zhang^a, Houxiang Sun^a, Qianqian Yu^a, Fan Yang^a, Qiaoxia Guo^b, Baojian Shen^{a,*}

^a State Key Laboratory of Heavy Oil Processing, The Key Laboratory of Catalysis of CNPC, College of Chemical Engineering, China University of Petroleum, No. 18 Fuxue Road, Changping, Beijing, 102249, PR China

^b College of Science, China University of Petroleum, No. 18 Fuxue Road, Changping, Beijing, 102249, China

ARTICLE INFO

Keywords:

Nitrogen-doped carbon materials
Electron-donating-accepting effect
Fe-bases catalysts
Hydrodesulfurization

ABSTRACT

Nitrogen-doped carbon (NDC) electron-donating materials were deposited on the surface of γ -Al₂O₃ as hybrid supports and then loaded with active metals to obtain Fe-based catalysts for dibenzothiophene (DBT) hydrodesulfurization (HDS). The unique electron-donating-accepting behavior between NDC materials and Fe species not only enhanced the dispersion of the active metals, but also enhanced the sulfidation degree of Fe atoms and the subsequent HDS reaction in comparison to the pure γ -Al₂O₃ supported catalysts. The HDS ratio of DBT at 400 °C improved from 36.9%–45.3% for pure FeS_x catalysts, and from 92.9%–98.8% for Fe₂Zn₃S_x catalysts. Furthermore, it was found that the donation of electrons from N to sulfided Fe species tuned the electron structure, which improved hydrogenation (HYD) pathway selectivity.

1. Introduction

Over the years, air pollution has emerged as a global environmental problem, and its mitigation has become a focus of the international community [1–3]. The combustion of fossil fuels, and in particular, the excessive use of transportation fuels such as gasoline and diesel, is one of the main sources of SO_x and causes acid rain and city acid fog, which are key contributors to air pollution. Most countries have imposed strict regulations to reduce the sulfur level in fuels [4–6]. Currently, traditional Co(Ni)-Mo(W) sulfide catalysts are still commonly used in the hydrodesulfurization (HDS) industry [7–11]. However, issues such as shortage of supplies, environmental toxicity, and exorbitant prices limit their further industrial applications. Iron (Fe) is a widely available, environmentally friendly, and inexpensive transition metal, which has therefore attracted research interest.

Although, previous studies have revealed that Fe is not suitable for the hydrotreating process, either as a single metal active phase (unsupported [12] or alumina-supported [13] FeS_x) or as an additive element (FeMo [14–17], FeW [18], or FeV [19]), our recent research found that the catalytic activity of Fe-based catalysts can be improved by approximately one order of magnitude by the assistance of zinc (Zn) [20]. The catalysts benefit from Zn as follows: 1) formation of a new active phase, FeZnS; and 2) excellent electron-donating capability of Zn

to Fe species. This is the only example that indicating electron-donating effect enhanced the catalytic HDS performance of Fe-based catalysts.

Nitrogen-doped carbon (NDC) was hailed as a material with immense research potential owing to its unique electronic properties [21–25]. The introduction of N with high charge and spin density into carbon materials endows them with electron-donating capability, thereby enhancing the catalytic performance of a series of catalysts, especially noble metals [21–27] and transition-metal (Co [28–30] and Fe [31–33]) oxides. The electron-donating NDC materials also strengthens the interaction between carbon materials and metal particles and improves the dispersion property of metal nanoparticles [21,24,25,28,34]. For active phase metals, electron-accepting and good dispersion properties are the key to enhance the HDS performance of Fe-based catalysts. Therefore, the development of NDC materials for the improvement of the HDS performance of Fe-based catalysts remains promising.

In this study, we employed NDC for Fe-based HDS catalysts, in an attempt to use the excellent electron-donating properties of NDC to ameliorate the dispersion and electronic environment of the Fe species, and thus improving its catalytic performance. An NDC coating was deposited on the surface of γ -Al₂O₃ through chemical vapor deposition (CVD) by using 1,10-phenanthroline as a raw material to obtain a relatively well-distributed network of nitrogen atoms as ‘active sites’.

* Corresponding author.

E-mail address: baojian@cup.edu.cn (B. Shen).

Subsequently, Fe (or Fe + Zn) oxides were loaded on the prepared hybrid support through incipient wetness impregnation followed by a presulfiding processes to obtain the sulfide catalysts. For comparison, γ -Al₂O₃ supported Fe-based catalysts were prepared similarly. The synergy effect due to the NDC coating on the Fe-based catalysts for DBT HDS was investigated.

2. Experimental

2.1. Preparation of catalysts

2.1.1. Preparation of supports

Pseudo-boehmite (JHN-03, Hejin Juhua Aluminum Company Ltd., China) was shaped by an extruder to form a clover extrudate, and then dried at 20 °C for 12 h and calcined in flowing air at 500 °C for 4 h to obtain γ -Al₂O₃. The γ -Al₂O₃ was crushed and sieved to obtain support particles in the range of 40–60 mesh.

Subsequently, 1.35 g of 1,10-phenanthroline (99 wt.%) was dissolved in 10 mL of anhydrous ethanol and added to a 5 g suspension of the prepared γ -Al₂O₃ particles. This was followed by drying at 20 °C for 12 h and calcination in flowing Ar at 600 °C for 2 h by the CVD method to obtain an NDC@ γ -Al₂O₃ support.

2.1.2. Preparation of oxide catalysts

All oxide catalysts were prepared by incipient wetness impregnation with Fe(NO₃)₃·9H₂O or Zn(NO₃)₂·6H₂O together as follows. First, a calculated amount of metal precursor was dissolved into anhydrous ethanol, and this solution was dropped on the surface of the previously prepared supports (γ -Al₂O₃ or NDC@ γ -Al₂O₃). Then, the samples were dried at 20 °C for 12 h and calcined in flowing Ar at 500 °C for 4 h to obtain oxide catalysts, for which the Fe₂O₃ loading of both pure Fe₂O₃ series catalysts and Fe₂Zn₃O₆ series catalysts were fixed at 8 wt.%; the Zn/(Fe + Zn) atomic ratios were 0 and 0.6. For reference, both MoO₃/ γ -Al₂O₃ and Fe-based catalysts supported on NDC@ γ -Al₂O₃ with different contents were also prepared using the same method. Specifically, the Fe₂O₃ loadings of both the pure Fe series and Fe-Zn series catalysts were 3 wt.% and 5 wt.%, respectively; the Zn/(Fe + Zn) atomic ratios were also 0 and 0.6, and the MoO₃ loading of the Mo-based catalyst was 8 wt.%.

2.2. Characterization of samples

X-ray diffraction (XRD) patterns of all the oxide catalysts were recorded on a PANalytical X'Pert Powder X-ray diffractometer using Cu K α radiation (40 kV, 40 mA). The samples were scanned from 10° to 80° with a scanning rate of 0.0065°/s.

The active phase contents of the oxide catalysts were characterized by X-ray fluorescence (XRF) using a PANalytical AxiosmAX instrument.

The bulk contents of carbon and nitrogen of the catalysts were measured by elemental analysis on a varioEL cube V2.0.1 instrument.

Nitrogen physical adsorption measurements were performed at –196 °C with a Micromeritics TriStar 3020 apparatus. All samples were vacuumized to degass and dehydrated at 350 °C for 8 h prior to the measurements. The total surface area (S_{BET}) was determined by the Brunauer-Emmett-Teller (BET) method. The pore size distribution and mesopore volume were calculated by the Barrett-Joyner-Halenda (BJH) adsorption branch of the isotherms. The total pore volumes (V_p) were estimated from the adsorbed amount at a relative pressure (P/P_0) of 0.98.

The morphology of all samples was observed using a Zeiss Gemini SEM 300 scanning electron microscope at an accelerating voltage of 5–20 kV. Transmission electron microscopy (TEM) images were recorded on a JEM-2100 transmission electron microscope operating at a

voltage of 200 kV. Energy dispersive X-ray spectroscopy (EDS) was performed to confirm the elemental contents of the samples. In order to prevent re-oxidation, all sulfide samples were prepared in a glove-box.

The H₂-TPR profiles of the oxide catalysts were obtained with a Micromeritics Autochem 2920 apparatus. Samples (200 mg) were loaded into a U-type quartz tube reactor and heated from 80 °C to 900 °C in 10% H₂/90% Ar flow. The heating rate and flow rate were 10 °C/min and 50 mL/min, respectively. The variation in gas concentration after reduction was monitored by a thermal conductivity detector (TCD).

The NH₃-TPD-MS profiles of the catalysts were also obtained with the Micromeritics Autochem 2920 apparatus. The samples (200 mg) were heated from room temperature to 600 °C at a rate of 10 °C/min and then cooled to 100 °C in a He flow. NH₃ was used as adsorbate and desorbed from 100 °C to 600 °C at a rate of 10 °C/min in He flow, the NH₃ desorption was detected by a Hiden QGA online mass spectrometer instead of the TCD detector in order to eliminate the influence of impurities.

Fourier transform infrared (FTIR) spectra of pyridine adsorbed on the catalysts were recorded in the range of 1400–1600 cm^{–1} on a MAGNA-IR 560 FT-IR spectrometer. The pyridine was adsorbed to pretreated samples at room temperature for 20 min. Then the sample was evacuated at 200 °C and 350 °C, and the spectrum was recorded.

X-ray photoelectron spectroscopy (XPS) measurements were used to measure the surface content and electron structure, and performed on a Thermo Fisher K-Alpha photoelectron spectrometer. The charging effect was minimized by using a charge neutralizer. The binding energies of all samples were revised using the carbon C 1s peak (284.6 eV) as a reference. To prevent re-oxidation, all sulfide samples were prepared in a glove-box that was connected to the XPS instrument.

2.3. Evaluation of catalytic performance

The HDS of DBT was carried out in a continuous-flow fixed-bed micro-reactor with an inner diameter of 8 mm and length of 420 mm. First, 1.00 g of catalyst (40–60 mesh) was loaded in the center of the reactor and sandwiched by quartz sand (40–60 mesh). Second, the oxide catalysts were pre-sulfided in situ by 10 vol.% CS₂ in *n*-decane as the sulfide feed under H₂ flow, 4.0 MPa, and 360 °C for 4 h. After presulfidation, a 50 mL *n*-decane solution with 0.58 wt.% DBT (sulfur content of 1 000 µg/g) was pumped into the reactor to remove the previous sulfide feed. The HDS reaction was performed under the following conditions: pressure of 4.0 MPa, reaction temperature of 360–400 °C, weight hourly space velocity (WHSV) of 8.4 h^{–1}, and H₂/hydrocarbon volumetric ratio of 300. The hydrocarbon product distribution was analyzed in an Agilent7890 gas chromatography (GC) system equipped with an MS 80 mass spectrometer. The total sulfur content was analyzed using a Zhonghuan RPP 2000SN sulfur-nitrogen analyzer. The HDS ratio was defined as:

$$\text{HDS ratio} = (1 - C_s/C_{s0}) \times 100\% \quad (1)$$

Where the HDS ratio is the percentage of sulfur removed, C_s is the total sulfur content of the corresponding product, and C_{s0} is the total sulfur content of the corresponding feed. In addition, by assuming a pseudo-first-order reaction for the HDS of DBT, the Fe-based catalyst activity can be expressed by the equation [7,20]:

$$k_{HDS} = \frac{F}{m} \ln \left(\frac{1}{1 - x} \right) \quad (2)$$

where k_{HDS} is the rate constant of HDS in mol/(g.s), x is the total conversion of DBT, F is the feeding rate of the reactant in mol/s, and m is the catalyst mass in g.

Table 1

Chemical compositions and textural properties of supports and oxide catalysts.

Sample	$S_{\text{BET}}^{\text{a}}$ (m^2/g)	APD ^b (nm)	$V_{\text{total}}^{\text{c}}$ (cm^{-3}/g)	$\text{Fe}_2\text{O}_3^{\text{d}}$ (wt.%)	ZnO^{d} (wt.%)	C content (wt.%)		N content (wt.%)	
						Surface ^e	Bulk ^f	Surface ^e	Bulk ^f
$\gamma\text{-Al}_2\text{O}_3$	360	14.9	0.843	–	–	–	–	–	–
NDC@ $\gamma\text{-Al}_2\text{O}_3$	332	11.3	0.811	–	–	15.18	4.76	1.00	0.59
$\text{Fe}_2\text{O}_3/\gamma\text{-Al}_2\text{O}_3$	311	11.3	0.771	8.1	–	–	–	–	–
$\text{Fe}_2\text{O}_3/\text{NDC@}\gamma\text{-Al}_2\text{O}_3$	260	17.5	0.871	8.1	–	12.70	1.96	0.57	0.34
$\text{Fe}_2\text{Zn}_3\text{O}_6/\gamma\text{-Al}_2\text{O}_3$	251	11.7	0.624	8.0	12.3	–	–	–	–
$\text{Fe}_2\text{Zn}_3\text{O}_6/\text{NDC@}\gamma\text{-Al}_2\text{O}_3$	210	17.5	0.651	8.1	12.3	11.93	1.70	0.44	0.29

^a BET surface area.^b Average pore diameter.^c Total pore volume.^d Measured by X-ray fluorescence (XRF).^e Measured by X-ray photoelectron spectroscopy (XPS).^f Measured by elemental analysis method.

3. Results and discussion

3.1. Characterization

3.1.1. Structure of oxide catalysts

The chemical composition and textural properties of the oxide catalysts are provided in Table 1. The contents of the loading metallic oxides (Fe_2O_3 and ZnO) of the oxide catalysts are close to the expected values. Both the surface and bulk contents of carbon and nitrogen were measured by XPS and elemental analysis method. The surface and bulk carbon contents of the hybrid support were 15.18% and 1.00%, respectively, and the nitrogen contents were 4.76% and 0.59%, respectively. This shows that the NDC material was successfully coated on the surface of $\gamma\text{-Al}_2\text{O}_3$. With the subsequent loading process of metallic oxides, both the surface and the bulk contents of carbon and nitrogen presented similar downward trends. This might be because, on the one hand, the loading of metallic oxides dilutes the content of the NDC material and, on the other hand, because of the loss of nitrogen during the heat treatment process.

The N_2 adsorption-desorption isotherms of the supports and oxide catalysts (Fig. 1) are similar and exhibit an evident hysteresis loop characteristic of a type IV isotherm. This indicates that all the samples are mesoporous materials. Owing to the NDC coating the external surface and pore channels of $\gamma\text{-Al}_2\text{O}_3$, the surface area, average pore size, and total pore volume of the hybrid support all show a downward trend. With the increase of metal oxide content, the textural properties

of the oxide catalysts prepared with pure $\gamma\text{-Al}_2\text{O}_3$ as support also show similarities in downward changes. In contrast, in the NDC@ $\gamma\text{-Al}_2\text{O}_3$ series catalysts, the average pore sizes exhibited an abnormal upward trend, which may reflect the presence of NDC materials changing the loading regimes of the metal oxide particles. Generally, the larger surface area and higher pore volume could provide sufficient space for the HDS reaction; furthermore, the larger pore diameters facilitate the diffusion of reactants and products over the catalysts [1,35–37]. Herein, with the introduction of NDC materials, the BET surface area of the pure Fe_2O_3 series and $\text{Fe}_2\text{Zn}_3\text{O}_6$ series catalysts are reduced by 16.4% and 16.3%, respectively, which is disadvantageous for DBT HDS reactions. However, both the total pore volume and average pore diameter of these two series catalysts showed upward trends. Particularly, the former improved by 13.0% and 4.3%, and the latter increased by 54.9% and 49.6%, which may result in the improved catalytic performance.

The powder XRD patterns of the supports and oxide catalysts are shown in Fig. 2. For the supports, the characteristic diffraction peaks of 37.6°, 45.8°, and 66.8° belong to $\gamma\text{-Al}_2\text{O}_3$ (PDF-29-0063) and are also retained in the hybrid NDC@ $\gamma\text{-Al}_2\text{O}_3$ support, and no distinct characteristic diffraction peaks of carbon materials are found, indicating that the introduction of NDC does not change the crystalline structure of $\gamma\text{-Al}_2\text{O}_3$. For the pure Fe-loaded catalysts (Fig. 2c and d), the diffraction peaks of 33.1° and 35.6° belong to Fe_2O_3 (PDF-89-0596). For the Fe and Zn co-loaded catalysts, diffraction peaks assigned to ZnO are not observed in patterns of $\text{Fe}_2\text{Zn}_3\text{O}_6/\gamma\text{-Al}_2\text{O}_3$ and $\text{Fe}_2\text{Zn}_3\text{O}_6/\text{NDC@}\gamma\text{-Al}_2\text{O}_3$ (Fig. 2e and f), implying that Zn species are more prone to form tiny crystallites (≤ 4 nm) or amorphous substances in the form of zinc oxides or Fe-Zn complex oxides, which would be well dispersed. In

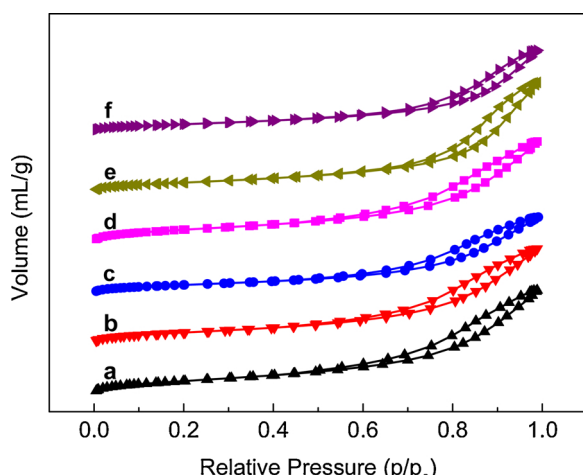


Fig. 1. N_2 adsorption-desorption isotherms of the supports and oxide catalysts. a) $\gamma\text{-Al}_2\text{O}_3$, b) $\text{Fe}_2\text{O}_3/\gamma\text{-Al}_2\text{O}_3$, c) $\text{Fe}_2\text{Zn}_3\text{O}_6/\gamma\text{-Al}_2\text{O}_3$, d) NDC@ $\gamma\text{-Al}_2\text{O}_3$, e) $\text{Fe}_2\text{O}_3/\text{NDC@}\gamma\text{-Al}_2\text{O}_3$, and f) $\text{Fe}_2\text{Zn}_3\text{O}_6/\text{NDC@}\gamma\text{-Al}_2\text{O}_3$.

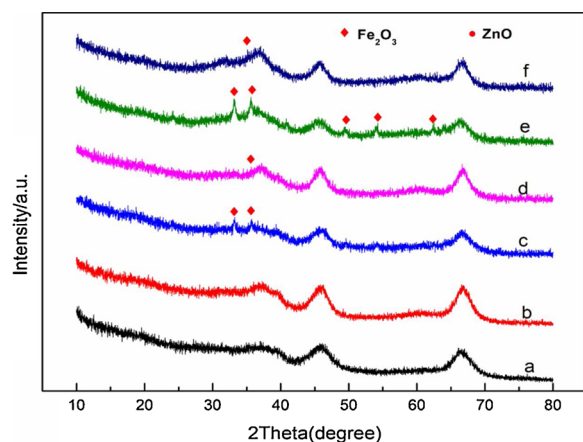


Fig. 2. X-ray diffraction patterns of supports and oxide catalysts. a) $\gamma\text{-Al}_2\text{O}_3$, b) NDC@ $\gamma\text{-Al}_2\text{O}_3$, c) $\text{Fe}_2\text{O}_3/\gamma\text{-Al}_2\text{O}_3$, d) $\text{Fe}_2\text{O}_3/\text{NDC@}\gamma\text{-Al}_2\text{O}_3$, e) $\text{Fe}_2\text{Zn}_3\text{O}_6/\gamma\text{-Al}_2\text{O}_3$, and f) $\text{Fe}_2\text{Zn}_3\text{O}_6/\text{NDC@}\gamma\text{-Al}_2\text{O}_3$.

Table 2

Amounts of acid sites and particle sizes of oxide catalysts, determined from pyridine-FTIR and XRD, respectively.

Sample	Amount of acid sites ($\mu\text{mol/g}$)				Particle size (nm)	
	200 °C		350 °C			
	L	B	L	B		
Fe ₂ O ₃ /γ-Al ₂ O ₃	147	0	90	0	43.21	
Fe ₂ O ₃ /NDC@γ-Al ₂ O ₃	71	0	43	0	4.66	
Fe ₂ Zn ₃ O ₆ /γ-Al ₂ O ₃	122	0	81	0	45.49	
Fe ₂ Zn ₃ O ₆ /NDC@γ-Al ₂ O ₃	68	0	54	0	5.43	

addition, the diffraction peaks of 33.1°, 35.6°, 49.4°, 54.0°, and 62.4° (shown in Fig. 2e and f) are all attributed to Fe₂O₃ (PDF-89-0596), and no characteristic diffraction peaks of Fe-Zn complex oxides were detected. The equivalent particle sizes of the samples are calculated from the broadening of the Fe₂O₃ (110) plane using Scherrer's equation, as shown in Table 2. With the introduction of the NDC material, the particle sizes of the pure Fe-loaded catalysts decreased from 43.21 nm to 4.66 nm, while the Fe-Zn co-loaded catalysts decreased from 45.49 nm to 5.43 nm. These results indicate the better dispersion of active phase metal oxides on the hybrid support of NDC@γ-Al₂O₃ than that on the pure γ-Al₂O₃ support.

The acidity of the samples is determined by pyridine adsorption and NH₃-TPD-MS (Table 2, Figure S1 and Figure S2 in the supporting information). The pyridine adsorption FTIR spectra, after degassing at 200 °C and 350 °C, are assigned to the total amounts of acid sites and the amounts of medium and strong acid sites, respectively. The bands at

1540 cm^{-1} and 1450 cm^{-1} are attributed to pyridine adsorbed onto Brønsted acid sites and Lewis acid sites [35,38,39]. The invisible band at 1540 cm^{-1} of the pyridine-FTIR spectra reveals that there is no detectable B acid site in these samples. Besides, with the introduction of the NDC material, the amounts of both total L acid sites and medium and strong L acid sites decreased by approximately half, which is consistent with the NH₃-TPD-MS results (see in Figure S2 in the supporting information). In view of the fact that the L acid is favorable for the hydrogenation ability of the catalysts and enhances the HDS activity [38], the decrease in the L acid amount proves the case in the negative; that is, the excellent electron-donating ability of NDC materials is the key factor to promote the HDS reaction.

Fig. 3 shows the surface morphology of the supports and oxide catalysts, indicating that the coating of filamentous carbon materials on the surface of γ-Al₂O₃ (Fig. 3b, d, f) is clearly different from the samples prepared by using pure γ-Al₂O₃ as the support (Fig. 3a, c, e). This not only proves that NDC materials were successfully deposited on the surface of the γ-Al₂O₃ support, but also proves that the subsequent loading of transition metal oxides did not damage the structure of NDC materials. This special filamentous structure may be caused by the catalysis effect of Fe contained in the γ-Al₂O₃ (see in Table S1 in the supporting information).

Fig. 4 shows representative TEM images (a-d) and corresponding particle size distributions (e-h) of the oxide catalysts. Distinct filamentous NDC materials can be observed in Fig. 4b and d, demonstrating that the loading of metal oxides does not alter or barely alters the NDC materials on the hybrid support. This is consistent with the SEM results. EDS scans were obtained to confirm that the nanoparticles are the target active-phase metal oxides (Figure S3 in the supporting information). There is a significant difference between the influence of

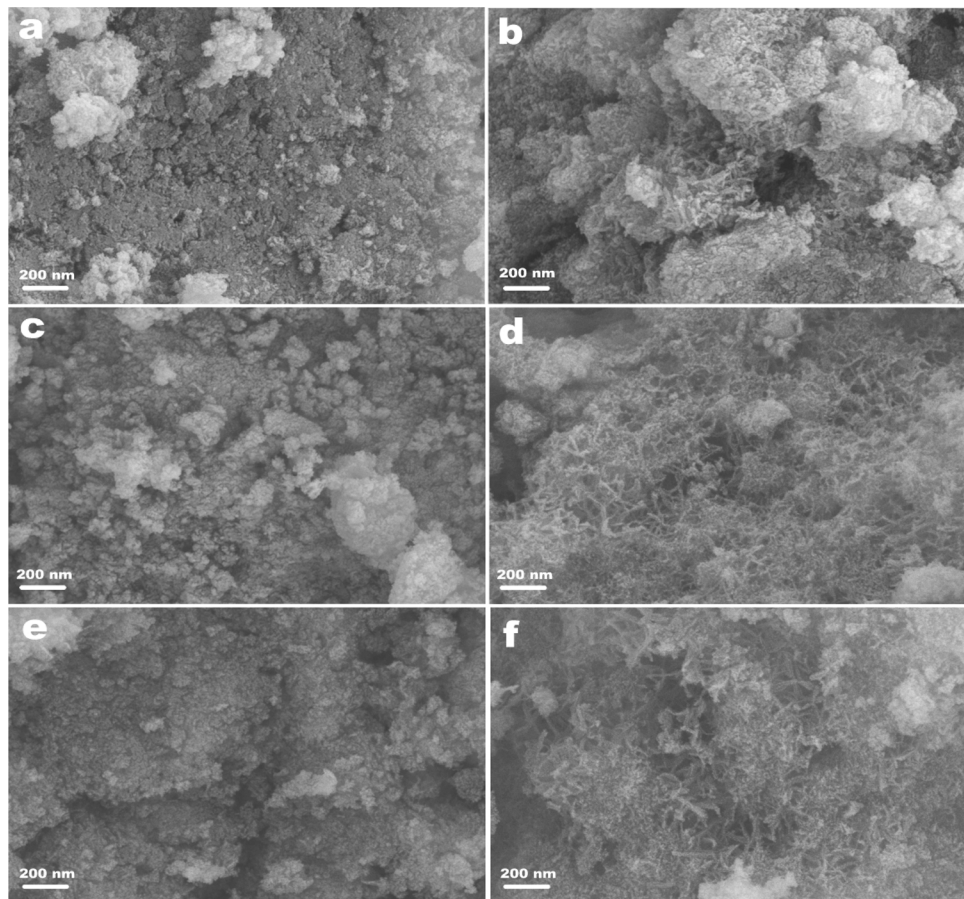


Fig. 3. SEM images of the supports and oxide catalysts. a) γ-Al₂O₃, b) NDC@γ-Al₂O₃, c) Fe₂O₃/γ-Al₂O₃, d) Fe₂O₃/NDC@γ-Al₂O₃, e) Fe₂Zn₃O₆/γ-Al₂O₃, and f) Fe₂Zn₃O₆/NDC@γ-Al₂O₃.

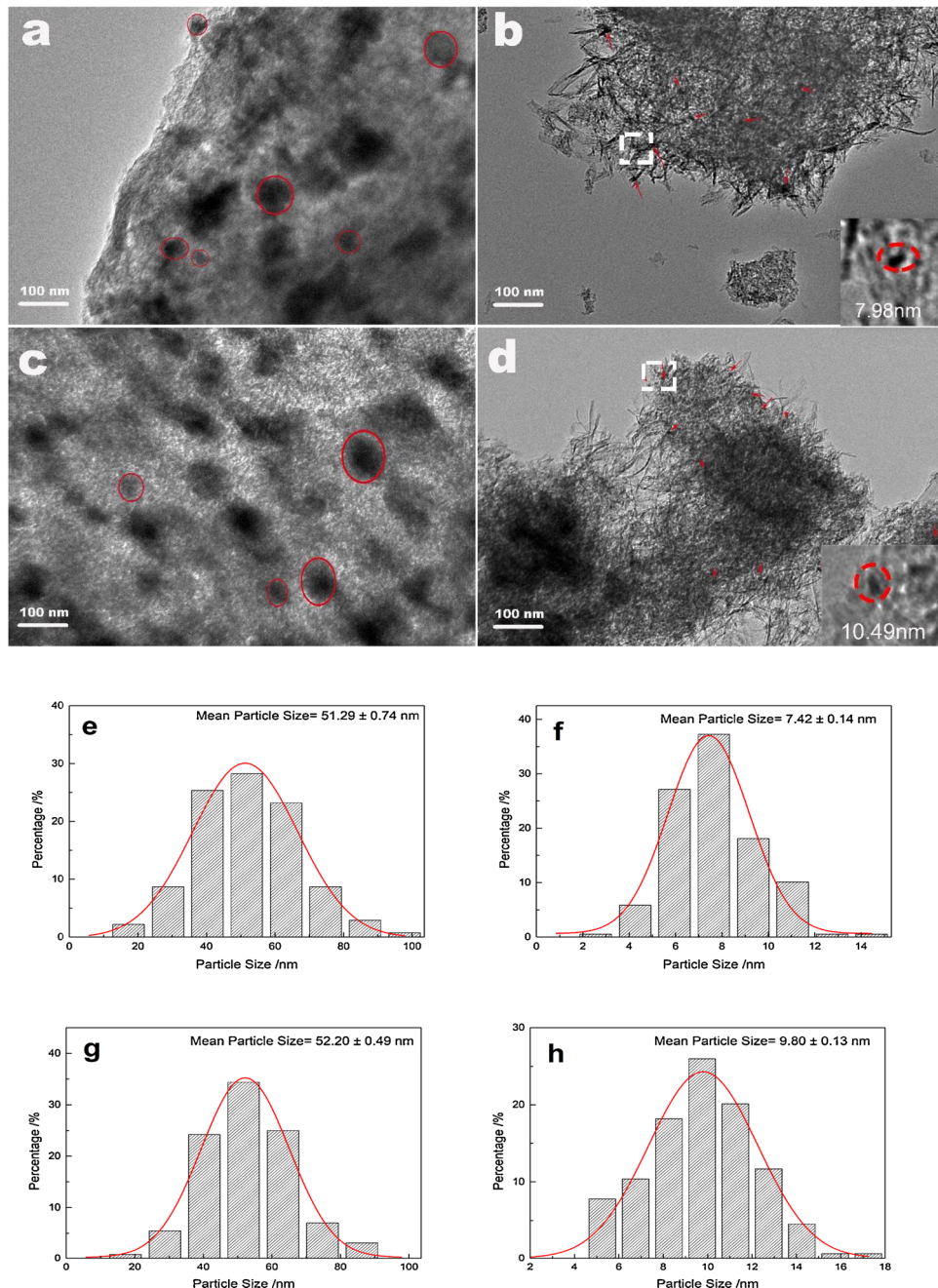


Fig. 4. Representative TEM images of the oxide catalysts; a) Fe₂O₃/γ-Al₂O₃, b) Fe₂O₃/NDC@γ-Al₂O₃, c) Fe₂Zn₃O₆/γ-Al₂O₃, d) Fe₂Zn₃O₆/NDC@γ-Al₂O₃. Particle size distributions of Fe₂O₃/γ-Al₂O₃; (e) Fe₂O₃/NDC@γ-Al₂O₃, (f) Fe₂Zn₃O₆/γ-Al₂O₃, and (g), Fe₂Zn₃O₆/NDC@γ-Al₂O₃ (h) obtained by measuring more than 100 particles.

pure γ-Al₂O₃ supports (Fig. 4a and c) and hybrid NDC@γ-Al₂O₃ supports (Fig. 4b and d) on the dispersion of active-phase metal oxide particles. Highly dispersed metal oxide nanoparticles smaller than 10 nm are observed in the series of hybrid support catalysts; in contrast, the particle sizes of the active-phase metal oxides in the catalysts supported on pure γ-Al₂O₃ are much larger. For the same support, ZnO only had a limited contribution towards the growth of metal oxide particles, indicating that the ZnO species are highly dispersed on the surface of the support; this is in agreement with the XRD results. More than 100 particles were selected to measure the particle size distribution of the metal oxide particles of each catalyst. Statistical analysis results are presented as histograms in Fig. 4e-h. Owing to the unique electron-donating properties of NDC materials and anchorage of the metal ions of the impregnation liquid on the hybrid supports prior to measurement, the mean particles sizes of the loading metal oxides decrease

sharply from 51.29 nm to 7.42 nm for Fe₂O₃ catalysts and from 52.20 nm to 9.80 nm for Fe₂Zn₃O₆ catalysts. Similar results were observed in Co/NCNTs [28] and Pt/NCNTs [24,25].

XPS was performed to reveal the structure types of the N sites and the electron interactions with the Fe species in the oxide catalysts. The N 1s spectrum of the NDC@γ-Al₂O₃ hybrid support is shown in Fig. 5. Only two components can be deconvoluted from the spectrum, representing N_P (pyridinic N, 398 eV) and N_{Pyr} (pyrrolic N, 399.7 eV) [40,41]. Among them, N_P accounts for 43.24% and N_{Pyr} for 56.76%. At present, the exact electronic effect mechanisms for different N site types in NDC materials to the noble metals of the catalysts are not fully understood. The biggest debate is between N_G (graphitic N) and N_P (pyridinic N), and there is little discussion of N_{Pyr}. Although objections are sometimes mentioned [42,43], the mainstream views propose that the higher dispersion of Pt NPs is caused by the donating effect of

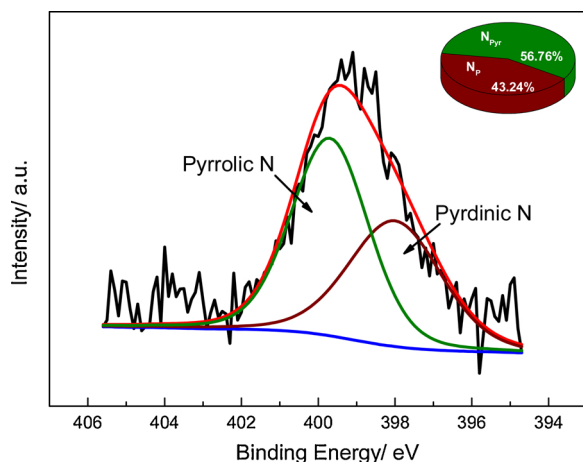


Fig. 5. XPS N 1s spectra of the NDC@ γ -Al₂O₃ hybrid support.

graphitic nitrogen, and N_p is regarded as an electron acceptor that interacts with the Pt NPs [21,44,45]. Strelko et al. [46] revealed that the band gaps of the materials mentioned here are 4.91 eV for N_p, 4.88 eV for carbon, 3.95 eV for N_{Gr}, and 2.98 eV for N_{Pyrr}. A lower band gap should lead to higher electron mobility and decreased electron work function. N_{Pyrr} has the highest electron mobility and the best electron donor properties. Meanwhile, this study targeted positively charged Fe species that have lost valence electrons, for which it is more difficult to lose electrons than it is for zero-valent Pt. In addition, compared with the Pt-N bond (0.228 nm and 1.70 eV), the shorter bond distance and higher bonding energy of the Fe-N bond (0.179 nm and 8.20 eV) indicate the stronger attracting electron ability of Fe species, with the same probe nitrogen source [47]. The above statement might forebode the electron-donating-accepting behavior between N and Fe species.

Electrons in the outer Fe 3p core level are more sensitive to electronic structure changes than are those in the inner Fe 2p core level [48]. Therefore, the Fe 3p spectra were chosen to analyze the electronic structure changes of Fe species in oxide catalysts. The Fe 3p spectra and N 1s spectra are shown in Fig. 6. The binding energies (BEs) of Fe 3p shift to lower values with the addition of NDC, for both the pure Fe₂O₃ series (from 56.4 eV to 55.9 eV) and Fe₂Zn₃O₆ series catalysts (from 56.0 eV to 55.8 eV), as shown in Fig. 6a and b. Meanwhile, compared with NDC@ γ -Al₂O₃, the N 1s BEs of Fe₂O₃/NDC@ γ -Al₂O₃ and Fe₂Zn₃O₆/NDC@ γ -Al₂O₃ shift to higher values (from 399.0 eV to 399.3 eV and 399.5 eV, respectively), as shown in Fig. 6c. Notably, with increasing metal oxide content, the height of the N 1s peak presents a decreasing trend owing to the coating of metal oxides on the surface of the catalysts. Simultaneously, in order to eliminate the influence of XPS detection limitations, catalysts with oxide contents of 3% and 5% (in terms of Fe₂O₃ contents, and molar ratio Zn/Fe + Zn = 0.6 for Fe-Zn co-loaded catalysts) were prepared and characterized by XPS. All of the Fe 3p bonding energies also shifted toward lower values. The chemical shifts reflect the electronic structure changes of the corresponding elements in the samples [48,49]. The above changes clearly reveal that electrons are transferred from N to Fe atoms, leading to an electron-rich state of the Fe atoms and electron-deficient state of the N atoms. An electron-rich state of Fe atoms implies that a lower density of core-level electrons of Fe nuclei participate in Fe-O covalent bond formation [50]. Consequently, the Fe-O bonds are weakened, and can be cleaved more easily during the subsequent reduction and sulfidation process.

In general, a good reducibility of active-phase metal oxide precursors in the HDS reaction implies a suitable interaction between the active metal and support, and the resulting facile formation of more active phases, which are essential for achieving high HDS activity [7,51–53]. Therefore, the reducibility of the Fe species was measured by H₂-TPR to analyze the effect of NDC addition on the active phases

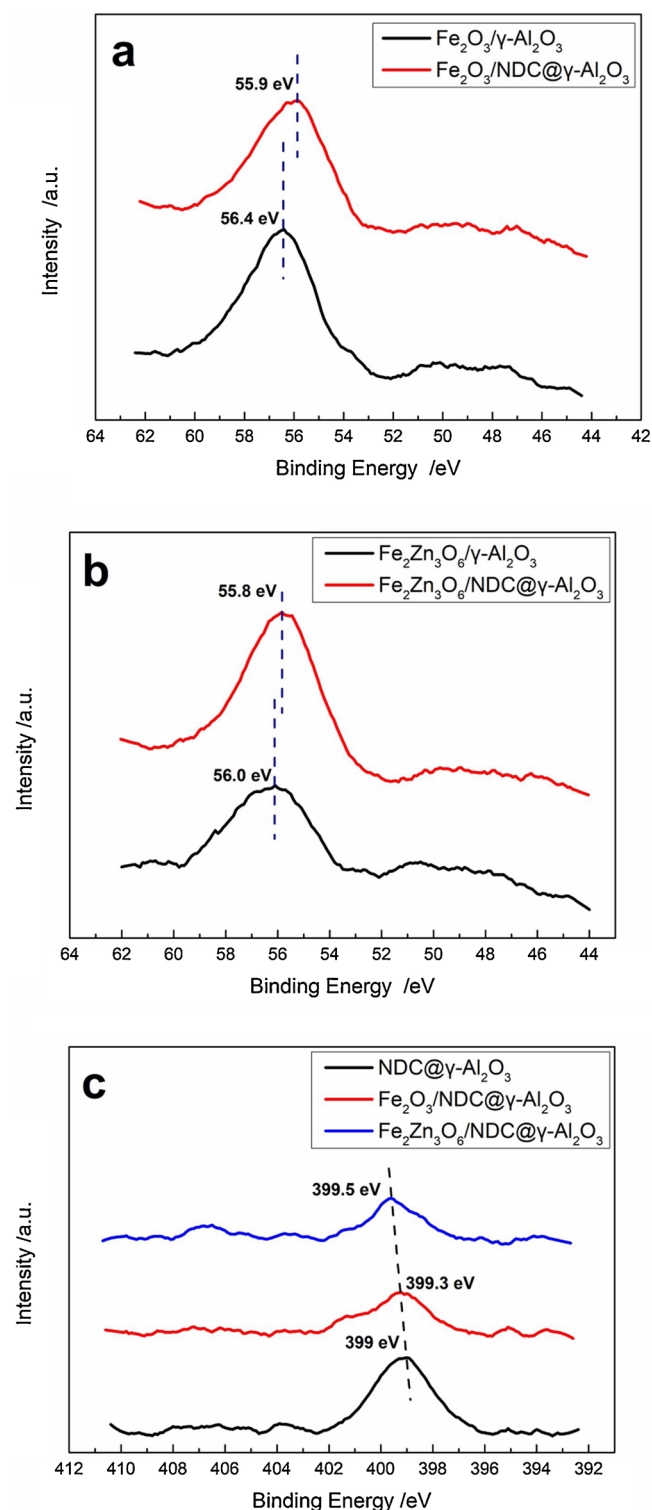


Fig. 6. XPS Fe 3p spectra of (a) pure Fe₂O₃ series catalysts and (b) Fe₂Zn₃O₆ series catalysts; (c) N 1s spectra of NDC@ γ -Al₂O₃, Fe₂O₃/NDC@ γ -Al₂O₃, and Fe₂Zn₃O₆/NDC@ γ -Al₂O₃.

(Fig. 7). Since the obtained H₂-TPR profiles were more complicated, peak-differentiation and imitation analyses were carried out to identify the positions of each peak more accurately. Three peaks (B–D) can be observed on the H₂-TPR profiles of the pure γ -Al₂O₃ series catalysts, whereas five peaks (A–E) appear on the H₂-TPR profiles of the hybrid series catalysts. The reduction of ZnO is typically considered to be negligible [54]; therefore, the assignments of all five peaks were based

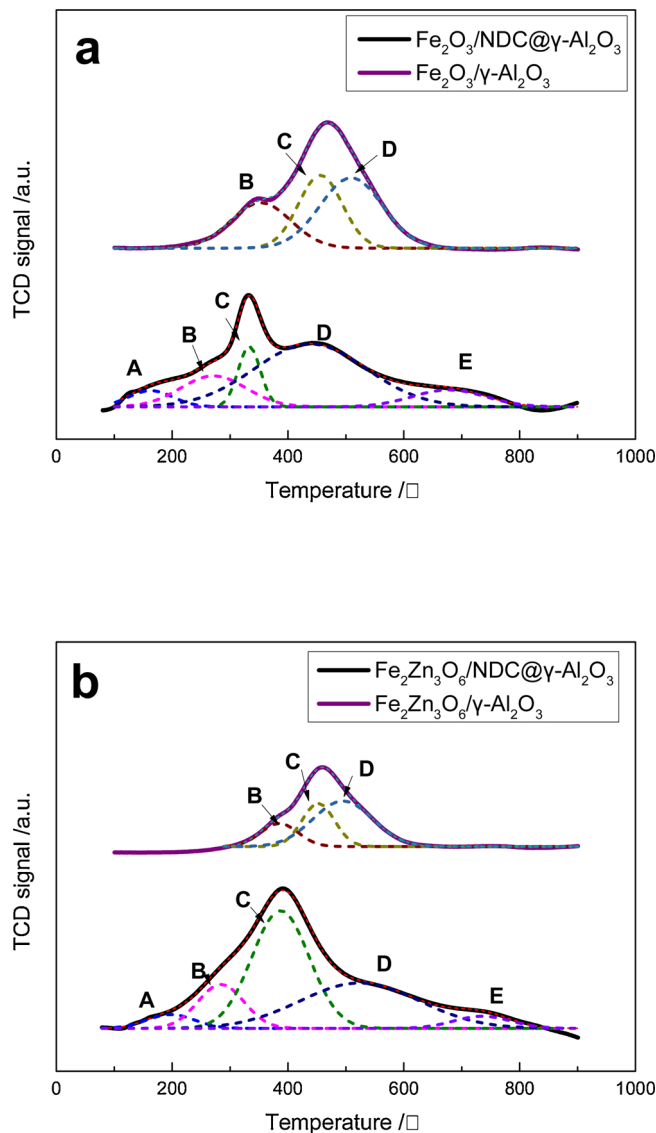


Fig. 7. H_2 -TPR profiles of (a) pure Fe_2O_3 series catalysts and (b) $\text{Fe}_2\text{Zn}_3\text{O}_6$ series catalysts.

Table 3
Reduction temperatures of catalysts based on H_2 -TPR analysis.

Catalyst	Peak A	Peak B	Peak C	Peak D	Peak E
$\text{Fe}_2\text{O}_3/\gamma\text{-Al}_2\text{O}_3$	–	350 °C	458 °C	513 °C	–
$\text{Fe}_2\text{O}_3/\text{NDC}@\gamma\text{-Al}_2\text{O}_3$	156 °C	270 °C	333 °C	446 °C	689 °C
$\text{Fe}_2\text{Zn}_3\text{O}_6/\gamma\text{-Al}_2\text{O}_3$	–	380 °C	452 °C	501 °C	–
$\text{Fe}_2\text{Zn}_3\text{O}_6/\text{NDC}@\gamma\text{-Al}_2\text{O}_3$	189 °C	286 °C	385 °C	521 °C	720 °C

on the contributions of Fe_2O_3 and NDC. Hence, peak A can be assigned to the reduction of the oxygen-containing groups of the NDC material; peaks B, C, and D can be assigned to the progressive reduction from Fe_2O_3 through Fe_3O_4 and FeO to metallic Fe [31,54–56]; and peak E corresponds to the gasification of NDC materials at approximately 700 °C [31,55]. The reduction temperatures for the four catalysts are shown in Table 3. Compared with Fe_2O_3 catalysts, the addition of NDC caused the reduction temperatures of peaks B, C, and D to decrease sharply from 350 °C to 270 °C, 458 °C to 333 °C, and 513 °C to 446 °C, respectively. Similarly, the main peak reduction temperatures for the $\text{Fe}_2\text{Zn}_3\text{O}_6$ catalysts also shift toward a lower temperature, from 380 °C

Table 4
Nitrogen and carbon contents of the sulfided catalysts.

Sample	N content (wt.%)		C content (wt.%)
	Surface ^a	Bulk ^b	Bulk ^b
$\text{FeS}_x/\gamma\text{-Al}_2\text{O}_3$	–	–	9.76
$\text{FeS}_x/\text{NDC}@\gamma\text{-Al}_2\text{O}_3$	0.38	0.14	10.51
$\text{Fe}_2\text{Zn}_3\text{S}_x/\gamma\text{-Al}_2\text{O}_3$	–	–	10.27
$\text{Fe}_2\text{Zn}_3\text{S}_x/\text{NDC}@\gamma\text{-Al}_2\text{O}_3$	0.16	0.13	11.28

^a Measured by XPS.

^b Measured by elemental analysis method.

to 268 °C and 452 °C to 385 °C. This indicates that the introduction of an NDC material improves the surface properties of the support and enables good interaction between the support and iron oxides, by which they can be reduced or sulfided more easily to generate more active phases; thus, achieving higher HDS activities.

3.1.2. Structure of sulfided catalysts

The carbon and nitrogen contents of the sulfided catalysts are shown in Table 4. Compared with the oxide catalysts (Table 1), the carbon contents of the sulfided catalysts present a large increasing trend, indicating carbon deposition during sulfidation. Meanwhile, both the surface and bulk nitrogen contents show a decreasing trend, attributable to the inevitable hydrodenitrification (HDN) process during sulfidation.

Representative TEM images of the sulfided catalysts are shown in Fig. 8. Compared with oxide catalysts, the morphologies of the sulfided catalysts significantly change. Fibrous carbon material is also observed on the surface of the sulfided pure $\gamma\text{-Al}_2\text{O}_3$ supported catalysts, owing to carbon deposited during sulfidation. Furthermore, although the mean particle size of FeS_x supported on the hybrid NDC@ $\gamma\text{-Al}_2\text{O}_3$ is smaller than that for support on the pure $\gamma\text{-Al}_2\text{O}_3$ (Figure S5 in the supporting information), the gap between them becomes smaller. This may be due to the rearrangement of active-phase metals during sulfidation [11], by which the Fe species supported on the hybrid NDC@ $\gamma\text{-Al}_2\text{O}_3$ can migrate and are enriched through thermal dynamical action. On the other hand, sulfur ions replace oxygen ions during sulfidation. A greater ionic radius of sulfur ions is not conducive to retaining the bulk structure of Fe species from the view of steric hindrance; therefore, the bulk Fe species are dissociated into smaller ones. A smaller particle size implies a greater percentage of surface atoms [48], which have a higher probability of contact with reactant molecules, thereby facilitating the HDS reaction.

For the traditional Co(Ni)-Mo(W) sulfided HDS catalysts, the high sulfidation degree, which implies that there are more active sites of the active phase, directly affects their catalytic activity [1,57–59]. However, there is no relevant literature on the calculation of the sulfidation degree for Fe-based sulfided catalysts. Using the principle employed for calculating the sulfidation degree of traditional catalysts [57,58] and considering the possible existence of Fe species during sulfidation, including un-reduced $\text{Fe}(\text{III})\text{-O}$, reduced $\text{Fe}(\text{II})\text{-O}$, sulfide FeS , FeS_2 , and FeZnS [20], the XPS profiles of $\text{Fe} 2p_{3/2}$ with fitted decomposition curves for the sulfided catalysts are presented in Fig. 9. The decomposition of the photopeaks shows five contributions, attributed to un-reduced $\text{Fe}(\text{III})\text{-O}$ ($2p_{3/2}$: 711.3 eV), reduced $\text{Fe}(\text{II})\text{-O}$ ($2p_{3/2}$: 708.4 eV), sulfided FeS ($2p_{3/2}$: 710.1 eV) and FeS_2 ($2p_{3/2}$: 706.9 eV), and FeZnS ($2p_{3/2}$: 709 eV) species of the $\text{Fe}_2\text{Zn}_3\text{S}_x$ series catalysts [20,60–63]. The sulfidation degree of the Fe species is defined as the approximate atomic ratio of the sum of FeS , FeS_2 , and FeZnS to the sum of $\text{Fe}(\text{III})\text{-O}$, $\text{Fe}(\text{II})\text{-O}$, FeS , FeS_2 , and FeZnS . The results from these photopeak decompositions are listed in Table 5. The sulfidation degree of the Fe species presents the following order: $\text{FeS}_x/\text{NDC}@\gamma\text{-Al}_2\text{O}_3$ (37%) < $\text{FeS}_x/\gamma\text{-Al}_2\text{O}_3$ (31%), $\text{Fe}_2\text{Zn}_3\text{S}_x/\text{NDC}@\gamma\text{-Al}_2\text{O}_3$ (48%) < $\text{Fe}_2\text{Zn}_3\text{S}_x/\gamma\text{-Al}_2\text{O}_3$ (46%). Owing to the introduction of NDC materials, the active-phase metal oxides are more susceptible to

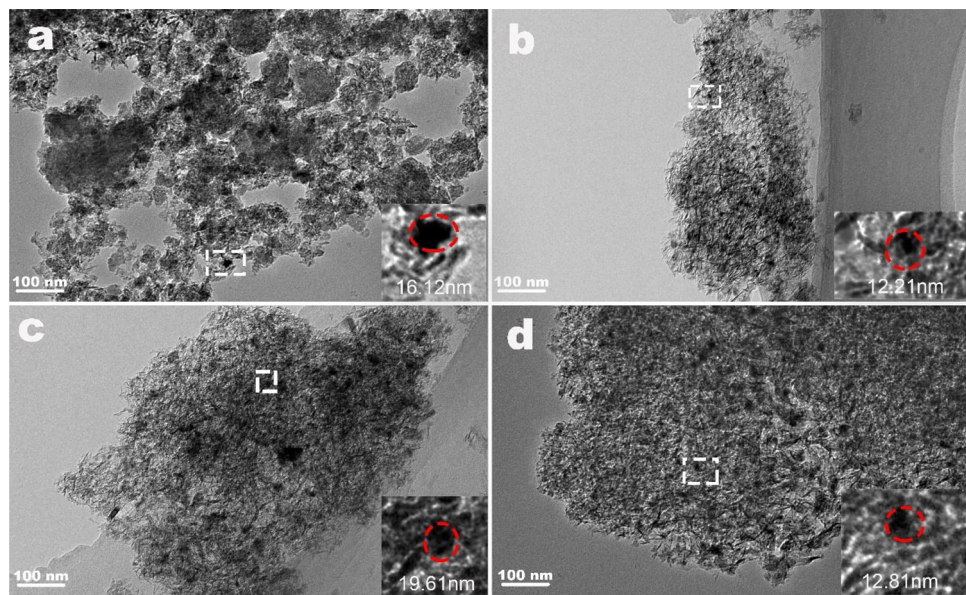


Fig. 8. Representative TEM images of the sulfided catalysts. (a) $\text{FeS}_x/\gamma\text{-Al}_2\text{O}_3$, (b) $\text{FeS}_x/\text{NDC}@\gamma\text{-Al}_2\text{O}_3$, (c) $\text{Fe}_2\text{Zn}_3\text{S}_x/\gamma\text{-Al}_2\text{O}_3$, and (d) $\text{Fe}_2\text{Zn}_3\text{S}_x/\text{NDC}@\gamma\text{-Al}_2\text{O}_3$.

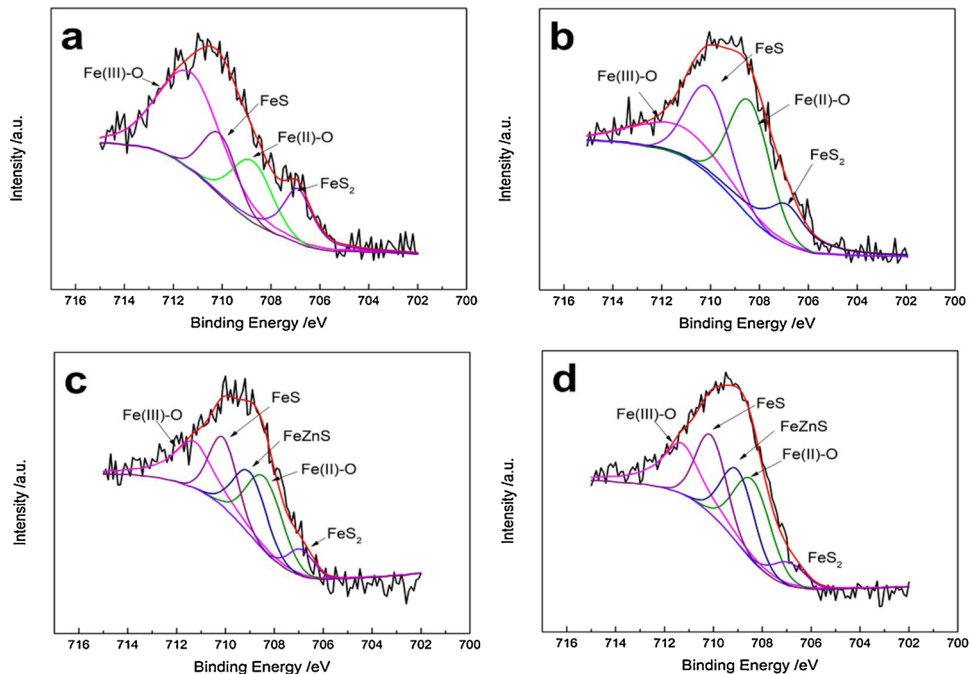


Fig. 9. $\text{Fe } 2\text{p}_{3/2}$ XPS spectra of sulfided catalysts at 360 °C with their fitted decomposition curves. (a) $\text{FeS}_x/\gamma\text{-Al}_2\text{O}_3$, (b) $\text{FeS}_x/\text{NDC}@\gamma\text{-Al}_2\text{O}_3$, (c) $\text{Fe}_2\text{Zn}_3\text{S}_x/\gamma\text{-Al}_2\text{O}_3$, and (d) $\text{Fe}_2\text{Zn}_3\text{S}_x/\text{NDC}@\gamma\text{-Al}_2\text{O}_3$.

Table 5
XPS data for catalysts sulfided at 360 °C.

Sample	Fe(III)-O /%	Fe(II)-O /%	FeS /%	FeS ₂ /%	FeZnS /%	Sulfidation degree /%
$\text{FeS}_x/\gamma\text{-Al}_2\text{O}_3$	51	18	15	16	–	31
$\text{FeS}_x/\text{NDC}@\gamma\text{-Al}_2\text{O}_3$	26	37	24	13	–	37
$\text{Fe}_2\text{Zn}_3\text{S}_x/\gamma\text{-Al}_2\text{O}_3$	27	27	19	7	20	46
$\text{Fe}_2\text{Zn}_3\text{S}_x/\text{NDC}@\gamma\text{-Al}_2\text{O}_3$	26	26	21	6	21	48

sulfidation, which confirms the results of XRD, TEM, $\text{H}_2\text{-TPR}$, and XPS characterizations of the oxide catalysts, and is therefore conducive to the improvement of HDS activity.

To investigate whether the sulfided Fe species and N species of the NDC coating still maintain electronic interaction after sulfidation, the

XPS profiles of the sulfided samples were collected (Fig. 10). The BEs of the $\text{Fe } 3\text{p}$ spectra of the samples still exhibit the tendency to shift to lower values (Fig. 10 and Figure S4 in the supporting information), particularly from 55.2 eV to 54.8 eV for FeS_x series catalysts and from 55.1 eV to 54.8 eV for $\text{Fe}_2\text{Zn}_3\text{S}_x$ series catalysts (Fig. 10a and b); this is

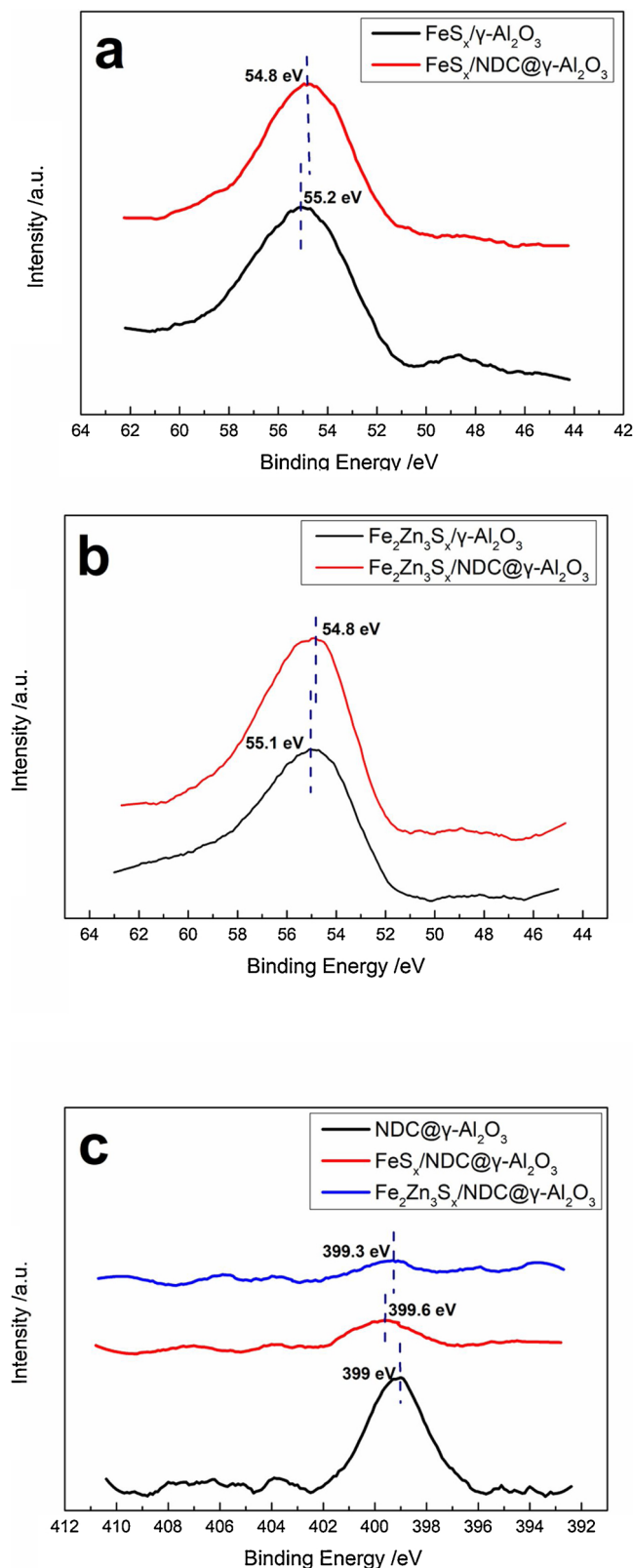


Fig. 10. Fe 3p XPS spectra of (a) FeS_x series catalysts; (b) Fe₂Zn₃S_x series catalysts; and (c) N 1s spectra of NDC@γ-Al₂O₃, FeS_x/NDC@γ-Al₂O₃ and Fe₂Zn₃S_x/NDC@γ-Al₂O₃.

aided by the addition of the NDC material. Simultaneously, compared with NDC@γ-Al₂O₃, the N 1s BEs of FeS_x/NDC@γ-Al₂O₃ and Fe₂Zn₃S_x/NDC@γ-Al₂O₃ catalysts show a tendency to shift toward higher values, from 399 eV to 399.6 eV and 399.3 eV (Fig. 10c). The above results are

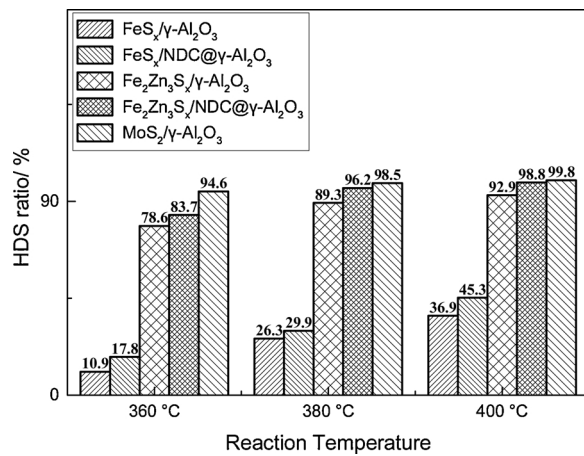


Fig. 11. The HDS ratio of DBT over the samples.

Table 6

Rate constant k_{HDS} for DBT HDS over four Fe-based catalysts and the path selectivity of HYD and DDS at 400 °C.

Catalyst	FeS _x /γ-Al ₂ O ₃	FeS _x /NDC@γ-Al ₂ O ₃	Fe ₂ Zn ₃ S _x /γ-Al ₂ O ₃	Fe ₂ Zn ₃ S _x /NDC@γ-Al ₂ O ₃
k_{HDS} ^a	0.34	0.43	1.92	2.41
BP ^b	88.6	81.2	58.3	52.5
THDBT + HHDBT ^b	1.0	0.9	2.9	1.9
CHB ^b	9.6	14.6	28.7	42.8
Benzyl-CP ^b	0.6	2.9	7.7	2.2
BCH ^b	~0.1	0.4	2.4	0.6
HYD/DDS ^b	0.13	0.23	0.71	0.90

^a Determined at about 30% of DBT conversion by changing the WHSV, reaction rate constant to 10^{-7} mol/(g.s).

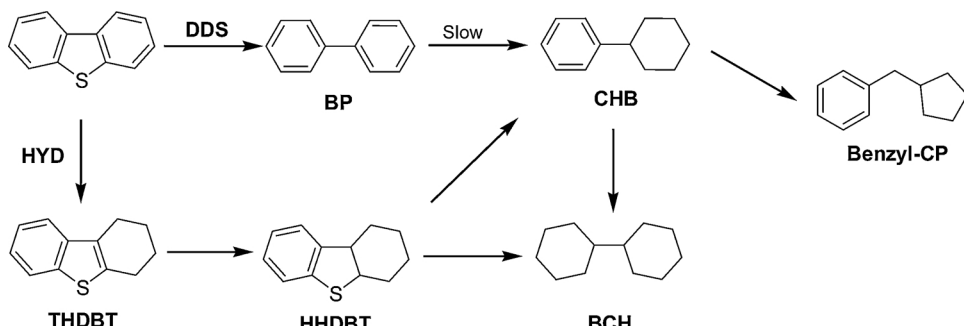
^b Determined at approximately 50% of DBT conversion by changing the WHSV.

evidence of electron transfer from the N species of the NDC material to the sulfided Fe species. To improve the HDS activity of Fe-based catalysts, receiving electrons is beneficial [20,64,65]. Therefore, the addition of an NDC electron-donating material is expected to improve the HDS activity of active phases of sulfided Fe species.

3.2. Evaluation of catalytic activity

All the catalysts, namely, 8 wt.% Fe₂O₃ and Zn/(Fe + Zn) in an atomic ratio of 0 and 0.6 loaded on pure γ-Al₂O₃ and hybrid NDC@γ-Al₂O₃ supports, respectively, and the reference Mo-based catalyst, were pre-sulfided by CS₂. The HDS activity of DBT was tested under the following conditions: 4.0 MPa, 360–400 °C, H₂/HC volumetric ratio of 300, and WHSV of 8.4 h⁻¹.

According to the results of the HDS ratio, rate constant k_{HDS} , and HYD/DDS ratios for DBT HDS over the Fe-based catalysts and MoS₂/γ-Al₂O₃ are shown in Fig. 11, Table 6, and Table S2 in supporting information. Overall, the HDS activity of the modified Fe-based catalysts made considerable progress, although it was slightly lower than that of the Mo-based catalyst (Fig. 11 and Table S2). Specifically, the HDS ratio of all zinc-added catalysts is significantly higher than those of pure Fe sulfide catalysts, the values for the Zn-added catalysts being 78.6%, 89.3%, and 92.9%, and those for the pure Fe sulfide catalysts being 10.9%, 26.3%, and 36.9% at 360, 380, and 400 °C, respectively, which is consistent with our recent research results [20]. The influence of the addition of NDC materials on the HDS activity of the catalysts presents the following trend: FeS_x/NDC@γ-Al₂O₃ > FeS_x/γ-Al₂O₃, and Fe₂Zn₃S_x/NDC@γ-Al₂O₃ > Fe₂Zn₃S_x/γ-Al₂O₃. Specifically, the introduction of NDC materials increases the DBT HDS ratio by 3.6%–8.4% for pure FeS_x catalysts at different temperatures, and 5.1%–6.9% for



Scheme 1. HDS reaction scheme of DBT.

$\text{Fe}_2\text{Zn}_3\text{S}_x$ catalysts. In addition, the rate constant k_{HDS} (Table 6) also increased from 0.34×10^{-7} mol/(g.s) to 0.43×10^{-7} mol/(g.s) for pure FeS_x catalysts at 400°C , and from 1.92×10^{-7} mol/(g.s) to 2.41×10^{-7} mol/(g.s) for $\text{Fe}_2\text{Zn}_3\text{S}_x$ catalysts. Thus, the addition of NDC electron-donating materials can effectively enhance the HDS activity of Fe-based catalysts, which satisfies our original design intention and correlates with previous characterization results of the catalysts.

In order to investigate the effect of the NDC materials on the abilities of hydrogenation and hydrogenolysis over the Fe-based catalysts, the DBT HDS products were detected by GC-MS (Table 6). The main products of the HDS reaction include direct desulfurization (DDS) molecules biphenyl (BP), hydrogenated S-containing molecules tetrahydro-DBT (THDBT) and hexahydro-DBT (HHDBT), bicyclohexyl (BCH), cyclohexylbenzene (CHB), and its isomer molecules benzylcyclopentane (Benzyl-CP). All catalyst products are similar to those obtained for traditional Co(Ni)-Mo(W) catalysts [11,20], which indicates that they may have a homologous reaction mechanism. The HDS mechanism of DBT can follow two parallel reaction routes, as shown in Scheme 1; the DDS route with the main product being BP, and the hydrogenation (HYD) pathway with the main products being THDBT, HHDBT, BCH, CHB, and Benzyl-CP. Since it is difficult to hydrogenate BP to CHB by Fe-based catalysts [20], it would be suitable to use the yield ratio of (1-BP)/BP to represent the selectivity of the HYD/DDS route. The results for route selectivity at 400°C are shown in Table 6. As we reported earlier [20], the introduction of Zn improved the selectivity of the HYD pathway, and the HYD/DDS ratio was promoted from 0.13 to 0.71 at 400°C . The HYD/DDS ratio of DBT over four catalysts follows the order: $\text{FeS}_x/\text{NDC}@\gamma\text{-Al}_2\text{O}_3 > \text{FeS}_x/\gamma\text{-Al}_2\text{O}_3$, and $\text{Fe}_2\text{Zn}_3\text{S}_x/\text{NDC}@\gamma\text{-Al}_2\text{O}_3 > \text{Fe}_2\text{Zn}_3\text{S}_x/\gamma\text{-Al}_2\text{O}_3$. Thus, modified NDC electron-donating materials clearly promote the selectivity of the HYD pathway by tuning the electronic environment of the active-phase FeS_x , enabling significant electron donation from N to the Fe species (Fig. 10), and tuning its electron structure to improve the adsorption of DBT and increase the HYD pathway selectivity [20,64–66].

4. Conclusion

In this work, NDC electron donor materials were coated on the surface of $\gamma\text{-Al}_2\text{O}_3$ as a hybrid support, which was obtained by pyrolysis of 1,10-phenanthroline. The main effects of the hybrid support toward the metal active-phase Fe species can be summarized as follows:

- The dispersion property of Fe species anchored to the surface of hybrid supports can be improved owing to the excellent electron-rich properties of NDC materials and electron donation from NDC materials to the Fe species.
- For the oxidation catalysts, the electron-donating effect of N to Fe led to an electron-rich state of the Fe atoms, which lowered the binding energy of Fe-O and easier bond breakage. This enhanced the sulfidation degree of the sulfided catalysts in the subsequent sulfidation, thereby increasing the amount of sulfided Fe species.

and improving the HDS activity of the catalysts.

- For sulfided catalysts, the electron transfer between NDC materials and sulfided Fe species improves the HDS activity of FeS_x . Furthermore, this increases the HYD pathway selectivity.

Thus, the addition of NDC electron donor materials can not only improve the dispersion and of Fe species, but also lead to a high sulfidation degree of the Fe atoms. Furthermore, owing to continuous electron transfer between them, it enhances the subsequent HDS reaction and improves HYD pathway selectivity by tuning the adsorption behavior of DBT. Thus, NDC materials are promising for designing low-cost Fe-based HDS catalysts for industrial refinery applications.

Acknowledgements

This work was supported by the National Natural Science Foundation of China (21776304), National Key R&D Program of China (2017YFB0306602), and PetroChina.

Appendix A. Supplementary data

Supplementary material related to this article can be found, in the online version, at doi:<https://doi.org/10.1016/j.apcatb.2019.05.011>.

References

- Y. Wang, C. Lancelot, C. Lamonier, F. Richard, K. Leng, Y. Sun, A. Rives, *ChemCatChem* 7 (2015) 3936–3944.
- R. Tian, B. Shen, F. Wang, C. Lu, C. Xu, *Energy Fuels* 23 (2009) 55–59.
- Y. Wang, B. Shen, K. Hao, J. Li, L. Wang, B. Feng, Q. Guo, *Catal. Commun.* 25 (2012) 59–63.
- C. Song, X. Ma, *Appl. Catal. B* 41 (2003) 207–238.
- A. Duan, G. Wan, Z. Zhao, C. Xu, Y. Zheng, Y. Zhang, T. Dou, X. Bao, K. Chung, *Catal. Today* 119 (2007) 13–18.
- D. Zhang, A. Duan, Z. Zhao, X. Wang, G. Jiang, J. Liu, C. Wang, M. Jin, *Catal. Today* 175 (2011) 477–484.
- Y. Fan, H. Xiao, G. Shi, H. Liu, Y. Qian, T. Wang, G. Gong, X. Bao, *J. Catal.* 279 (2011) 27–35.
- L.V. Haandel, G.M. Bremmer, E.J.M. Hensen, T. Weber, *J. Catal.* 351 (2017) 95–106.
- N.Y. Topsøe, H. Topsøe, *J. Catal.* 84 (1983) 386–401.
- S.P.A. Louwers, R. Prins, *J. Catal.* 139 (1993) 525–539.
- H. Sun, Q. Wang, X. Zhang, Q. Yu, L. Li, Y. Wang, B. Shen, *Appl. Catal. A Gen.* 563 (2018) 137–145.
- T.A. Pecoraro, R.R. Chianelli, *J. Catal.* 67 (1981) 430–445.
- J. Quarararo, S. Mignard, S. Kasztelan, *J. Catal.* 192 (2000) 307–315.
- W.L.T.M. Ramselaar, M.W.J. Crajé, R.H. Hadders, E. Gerkema, V.H.J.D. Beer, A.M.V.D. Kraan, *Appl. Catal.* 65 (1990) 69–84.
- W.L.T.M. Ramselaar, R.H. Hadders, E. Gerkema, *Appl. Catal.* 51 (1989) 263–283.
- W.L.T.M. Ramselaar, M.W.J. Crajé, E. Gerkema, R.H. Hadders, J.J.V. Loef, V.H.J.D. Beer, A.M.V.D. Kraan, *Hyperfine Interact.* 41 (1988) 697–700.
- M. Karroua, J. Ladrière, H. Matralis, P. Grange, B. Delmon, *J. Catal.* 138 (1992) 640–658.
- Y. Villasana, F. Ruscio-Vanalesti, C. Pfaff, F.J. Méndez, M.A. Luis-Luis, J.L. Brito, *Fuel* 110 (2013) 259–267.
- B.P. Embaid, F. Gonzalez-Jimenez, C.E. Scott, *Appl. Catal. A Gen.* 287 (2005) 75–82.
- H. Li, J. Liu, J. Li, Y. Hu, W. Wang, D. Yuan, Y. Wang, T. Yang, L. Li, H. Sun, S. Ren, X. Zhu, Q. Guo, X. Wen, Y. Li, B. Shen, *ACS Catal.* 7 (2017) 4805–4816.

[21] X. Ning, H. Yu, F. Peng, H. Wang, *J. Catal.* 325 (2015) 136–144.

[22] Z. Lei, L. An, L. Dang, M. Zhao, J. Shi, S. Bai, Y. Cao, *Microporous Mesoporous Mater.* 119 (2009) 30–38.

[23] R. Arrigo, M.E. Schuster, Z. Xie, Y. Yi, G. Wowsnick, L.L. Sun, K.E. Hermann, M. Friedrich, P. Kast, M. Hävecker, A. Knop-Gericke, R. Schlögl, *ACS Catal.* 5 (2015) 2740–2753.

[24] X. Ning, Y. Li, B. Dong, H. Wang, H. Yu, F. Peng, Y. Yang, *J. Catal.* 348 (2017) 100–109.

[25] B. Zhang, D.S. Su, *ChemCatChem* 7 (2015) 3639–3645.

[26] P. Chen, L.M. Chew, W. Xia, *J. Catal.* 307 (2013) 84–93.

[27] K. Chizari, I. Janowska, M. Houllé, I. Florea, O. Ersen, T. Romero, P. Bernhardt, M.J. Ledoux, C. Pham-Huu, *Appl. Catal. A Gen.* 380 (2010) 72–80.

[28] P. Chen, F. Yang, A. Kostka, W. Xia, *ACS Catal.* 4 (2014) 1627–1636.

[29] C. Xu, M. Lu, B. Yan, Y. Zhan, P. Balaya, L. Lu, J. Lee, *ChemSusChem* 9 (2016) 3067–3073.

[30] B. Zheng, J. Wang, F.B. Wang, X.H. Xia, *J. Mater. Chem. A* 2 (2014) 9079–9084.

[31] J. Lu, L. Yang, B. Xu, Q. Wu, D. Zhang, S. Yuan, Y. Zhai, X. Wang, Y. Fan, Z. Hu, *ACS Catal.* 4 (2014) 613–621.

[32] H.J. Schulte, B. Graf, W. Xia, M. Muhler, *Chemcatchem* 4 (2012) 350–355.

[33] R.V. Jagadeesh, K. Natte, H. Junge, M. Beller, *ACS Catal.* 5 (2015) 1526–1529.

[34] S. Armenise, L. Roldán, Y. Marco, A. Monzón, E. García-Borjé, *J. Phys. Chem. C* 116 (2012) 26385–26395.

[35] D. Gao, A. Duan, X. Zhang, Z. Zhao, H. E, J. Li, H. Wang, *Appl. Catal. B* 165 (2015) 269–284.

[36] S. Song, X. Zhou, A. Duan, Z. Zhao, K. Chi, M. Zhang, G. Jiang, J. Liu, J. Li, X. Wang, *Microporous Mesoporous Mater.* 226 (2016) 510–521.

[37] X. Wang, J. Mei, Z. Zhao, P. Zheng, Z. Chen, J. Li, J. Fan, A. Duan, C. Xu, *Ind. Eng. Chem. Res.* 56 (2017) 10018–10027.

[38] Y. Li, D. Pan, C. Yu, Y. Fan, X. Bao, *J. Catal.* 286 (2012) 124–136.

[39] T. Kataoka, J.A. Dumesic, *J. Catal.* 112 (1988) 66–79.

[40] Y. Cao, H. Yu, J. Tan, F. Peng, H. Wang, J. Li, W. Zheng, N. Wong, *Carbon* 57 (2013) 433–442.

[41] Z. Chen, D. Higgins, H.S. Tao, R.S. Hsu, Z. Chen, *J. Phys. Chem. C* 113 (2009) 21008–21013.

[42] X. Tuaev, J.P. Paraknowitsch, R. Illgen, A. Thomas, P. Strasser, *J. Chem. Soc. Faraday Trans.* 14 (2012) 6444–6447.

[43] L. Jia, D.A. Bulushev, O.Y. Podyacheva, A.I. Boronin, L.S. Kibis, E.Y. Gerasimov, S. Beloshapkin, I.A. Seryak, Z.R. Ismagilov, J.R.H. Ross, *J. Catal.* 307 (2013) 94–102.

[44] Y. Chen, J. Wang, H. Liu, M.N. Banis, R. Li, X. Sun, T.K. Sham, S. Ye, S. Knights, *J. Phys. Chem. C* 115 (2011) 3769–3776.

[45] A.H. Nevidomskyy, G. Csányi, M.C. Payne, *Phys. Rev. Lett.* 91 (2003) 105502.

[46] V.V. Strelko, V.S. Kuts, P.A. Thrower, *Carbon* 38 (2000) 1499–1524.

[47] H. Feng, J. Ma, Z. Hu, *J. Mater. Chem.* 20 (2010) 1702–1708.

[48] H. Suo, S. Wang, C. Zhang, J. Xu, B. Wu, Y. Yang, H. Xiang, Y. Li, *J. Catal.* 286 (2012) 111–123.

[49] W.E. Kaden, T. Wu, W.A. Kunkel, S.L. Anderson, *Science* 326 (2009) 826–829.

[50] S. Qin, C. Zhang, J. Xu, H. Xiang, Y. Li, *Appl. Catal. A Gen.* 392 (2011) 118–126.

[51] C.M. Wang, T.C. Tsai, I. Wang, *J. Catal.* 262 (2009) 206–214.

[52] B. Scheffer, P. Molhoek, J.A. Moulijn, *Appl. Catal.* 46 (1989) 11–30.

[53] Y. Fan, X. Bao, H. Wang, C. Chen, G. Shi, *J. Catal.* 245 (2007) 477–481.

[54] M. Liang, W. Kang, K. Xie, *J. Nat. Gas Chem.* 18 (2009) 110–113.

[55] R.M.M. Abbaslou, A. Tavassoli, J. Soltan, A.K. Dalai, *Appl. Catal. A Gen.* 367 (2009) 47–52.

[56] W. Ma, E.L. Kugler, J. Wright, D.B. Dadyburjor, *Energy Fuels* 20 (2006) 2299–2307.

[57] A. Duan, T. Li, Z. Zhao, B. Liu, X. Zhou, G. Jiang, J. Liu, Y. Wei, H. Pan, *Appl. Catal. B* 165 (2015) 763–773.

[58] G. Wan, A. Duan, Y. Zhang, Z. Zhao, G. Jiang, D. Zhang, Z. Gao, J. Liu, K.H. Chung, *Energy Fuels* 23 (2009) 3846–3852.

[59] K.B. Tayeb, C. Lamonier, C. Lancelot, M. Fournier, A. Bonduelle-Skrzypczak, F. Bertoncini, *Appl. Catal. B* 126 (2012) 55–63.

[60] G.A. Bukhtiyarova, V.I. Bukhtiyarov, N.S. Sakaeva, V.V. Kachev, B.P. Zolotovskii, *J. Mol. Catal. A Chem.* 158 (2000) 251–255.

[61] M.C. Biesinger, B.P. Payne, A.P. Grosvenor, L.W.M. Lau, A.R. Gerson, R.S.C. Smart, *Appl. Surf. Sci.* 257 (2011) 2717–2730.

[62] A.M. Widler, T.M. Seward, *Geochim. Cosmochim. Acta* 66 (2002) 383–402.

[63] B. Hua, B. Deng, *Environ. Sci. Technol.* 42 (2008) 8703–8708.

[64] M. Ramos, G. Berhault, D.A. Ferrer, B. Torres, R.R. Chianelli, *Catal. Sci. Technol.* 2 (2012) 164–178.

[65] M. Lacroix, C. Guillard, M. Breysse, M. Vrinat, T.D. Courières, *J. Catal.* 135 (1992) 304–309.

[66] R. Hubaut, *Appl. Catal. A Gen.* 322 (2007) 121–128.